An EV-Scale Demonstration of In-Situ Battery Electrochemical Impedance Spectroscopy and BMS-Limited Pack Performance Analysis

Zhe Gong, *Member, IEEE*, Avram Kachura, Seyed Amir Assadi, *Student Member, IEEE*, Nicholas Cusimano, Joshua Piruzza, James Xu, and Olivier Trescases, *Senior Member, IEEE*

***Abstract*—State-of-power (SOP) and state-of-charge (SOC) estimation inaccuracy manifests throughout the electric vehicle (EV) battery lifetime due to the nonlinear degradation trajectory that is unique to each use-case. The inaccuracy leads to premature termination of charge and discharge operations, which results in the virtual loss of battery performance. In-situ electrochemical impedance spectroscopy (EIS) has been proposed to provide real-time battery impedance measurements, which can theoretically improve the SOP/SOC estimation accuracy. In this work, an EV-scale in-situ EIS system is demonstrated experimentally, from impedance measurement to equivalent circuit model (ECM) extraction. The pack-level discharge energy versus SOP/SOC estimation errors is also simulated, which quantifies the virtual loss of battery performance. The measured-impedance error tolerance of three common ECM extraction techniques is then examined through a randomized set of simulated EIS tests with injected measurement noise. Finally, in-situ impedance measurement is performed on 20 battery submodules using an electric pickup truck EIS system. The ECM-predicted voltage output is compared against measured driving data. Experimental results indicate approximately 8%–9% improvement in SOP estimation accuracy at 3 °C and 10 °C between the in-situ extracted models and a representative baseline.**

***Index Terms*—Battery management systems (BMSs), electric vehicles (EVs), electrochemical impedance spectroscopy (EIS), equivalent circuits, lithium-ion batteries.**

I. Introduction

IN 2021, 6.6 million new electric vehicle (EV) registrations were recorded worldwide, corresponding to a 100% growth in one year [1]. Sustaining the fast growth of EV deployment is crucial to the continued reduction of greenhouse gas emissions, and dependent on advances in lithium-ion battery technology. In particular, the cost of batteries must be reduced without sacrificing safety and energy/power density. A core component of EV battery systems is the battery management system (BMS), as shown in Fig. 1(a). The BMS is typically responsible for the following:

1) cell voltage/temperature/current sensing;
2) state-of-charge (SOC), state-of-power (SOP), and state-of-health/remaining-capacity (SOH) estimation [2], [3], [4];
3) cell balancing [5].

The estimated SOC and SOP of a battery pack restrict the battery pack charging and discharging capability. Without accurate SOP/SOC estimation accuracy, the battery pack capacity and power utilization must be virtually limited to avoid over and undervoltage. A recent example is the GM Bolt virtual 90%-SOC constraint, which was imposed to limit the risk of battery fire [6].

The cell model identification and SOP estimation process studied in this work is shown in Fig. 1(b). An in-situ electrochemical impedance spectroscopy (EIS) system generates cell impedance measurements while the vehicle is at zero

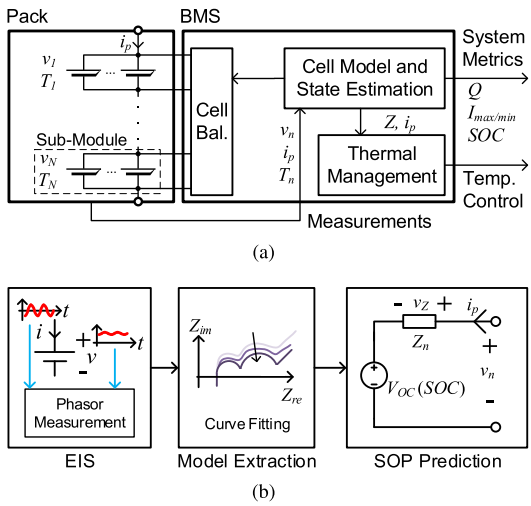

Fig. 1. Impedance-based EV battery management. (a) Typical battery pack and BMS architecture. (b) Cell modeling and state estimation process studied in this work, which incorporates in-situ EIS.

Manuscript received 13 June 2022; revised 10 September 2022; accepted 6 October 2022. Date of publication 25 October 2022; date of current version 3 April 2023. This work was supported by Litens Automotive Partnership and the Ontario Centre of Innovation. *(Corresponding author: Zhe Gong.)*

The authors are with the Edward S. Rogers Sr. Department of Electrical and Computer Engineering, University of Toronto, Toronto ON M5S, Canada (e-mail: zhe.gong@mail.utoronto.ca; avram.kachura@mail.utoronto.ca; amir.assadi@mail.utoronto.ca; nicholas.cusimano@mail.utoronto.ca; joshua.piruzza@mail.utoronto.ca; jameszn.xu@mail.utoronto.ca; ot@ece.utoronto.ca).

Color versions of one or more figures in this article are available at https://doi.org/10.1109/TIE.2022.3215833.

Digital Object Identifier 10.1109/TIE.2022.3215833

0278-0046 © 2022 IEEE. Personal use is permitted, but republication/redistribution requires IEEE permission.
See https://www.ieee.org/publications/rights/index.html for more information.

Authorized licensed use limited to: Sungkyunkwan University. Downloaded on August 18,2025 at 04:23:47 UTC from IEEE Xplore. Restrictions apply.

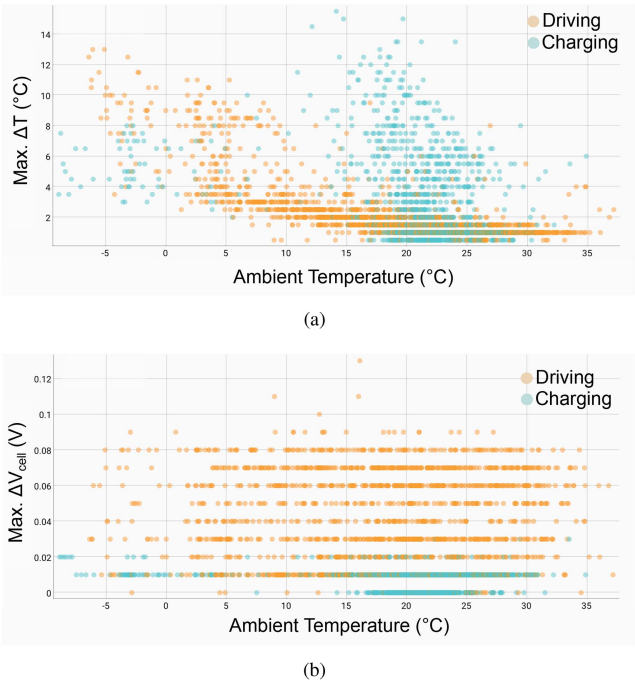

Fig. 2. Challenges in battery modeling and SOP estimation. (a) Maximum cell temperature variation. (b) Maximum cell-to-cell voltage difference, both measured from a commercial EV at −10 to 40 °C.

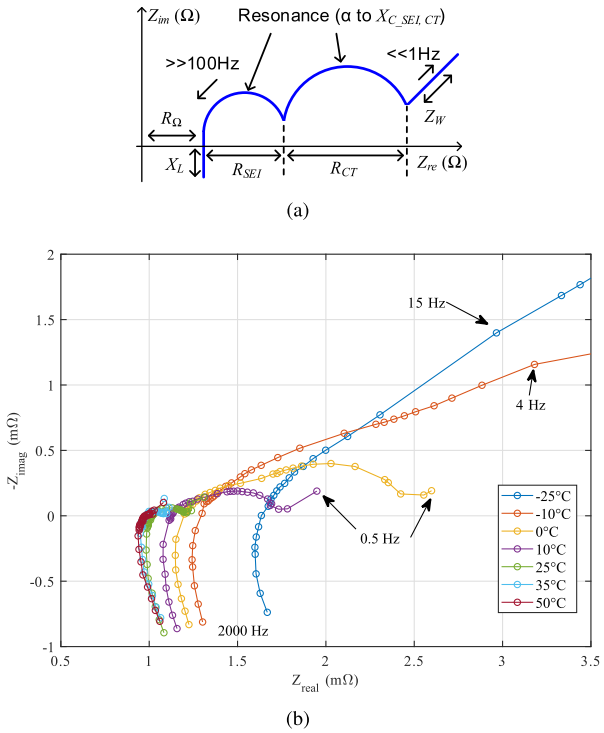

Fig. 3. Lithium battery impedance: (a) theoretical Nyquist curve, (b) measured impedance of a 44Ah Lithium NMC battery cell.

speed. Curve-fitting is used to match the impedance of an equivalent circuit model (ECM) to the measured impedance. An example lumped-impedance ECM, including a voltage source modeling the SOC-dependent cell electromotive force (EMF) is shown in Fig. 1(b). The nonlinear battery behavior across varying temperature, SOC, and degradation must be captured in the model identification and state estimation procedures. The maximum instantaneous cell-to-cell temperature and voltage deviation of a commercial EV battery pack are shown in Fig. 2, at various operating temperatures. Charging events occur primarily near room temperature, and the cell temperatures vary due to high heat production and uneven cooling across the battery pack. During cold temperature driving, the pack power is generally lower than charging, but cell temperature variations still arise due to uneven heating. Meanwhile, the cell-to-cell voltage deviation, which represents the difference in cell overpotentials, varies more during driving than charging due to transient power flow. The commercial EV measurements demonstrate the temperature-dependent nonlinear impedance that must be captured in the BMS.

Existing methods for model parameter identification and SOP estimation typically capture the battery voltage-to-current response using a generalized function to describe the cell overpotential. Various algorithms have been proposed to capture the battery nonlinearity using the measured battery voltage, current, and temperature during operation. These methods target stable SOP prediction with an LTI battery model, while implementing a secondary algorithm to introduce time-dependent model nonlinearity. Specific implementations include the following:

1) the use of a linear parameter varying (LPV) model structure where the resistance of an ECM is varied according to temperature [7];
2) coupling an ECM-based LPV model with model-predictive control to support long time-horizon battery SOP predictions [8];
3) ECM state and parameter coestimation using feedback-based state observers [9].

These schemes are limited by the need to ensure the algorithm stability. According to [7], the challenges include the following:

1) the algorithm sensitivity to the initial model conditions;
2) estimation errors arising from computation and measurement timing mismatch;
3) instability related to the low fidelity of cell temperature estimates, which are based on module-level measurements;
4) voltage response error compensation by the wrong model subcomponents (e.g., preventing SOC-related voltage error being compensated by capacitive element voltage corrections).

The lithium-ion battery thermal and electrical behavior are related to the EV operating conditions through the battery electrical impedance [4], [10]. An idealized lithium-ion battery impedance Nyquist plot is shown in Fig. 3(a). Across the frequency range, the battery impedance describes the following:

1) the build-up of the solid-electrolyte interphase (R_{SEI}, $X_{C,\text{SEI}}$);
2) the charge transfer behavior during ion intercalation and deintercalation (R_{CT}, $X_{C,\text{CT}}$);
3) the mass-transport process in the active materials of the electrodes due to changes in the electrochemical potential (Z_W);
4) the ohmic resistance of the cell (R_Ω);
5) the parasitic inductance arising from conductor geometry (X_L).

Authorized licensed use limited to: Sungkyunkwan University. Downloaded on August 18,2025 at 04:23:47 UTC from IEEE Xplore. Restrictions apply.

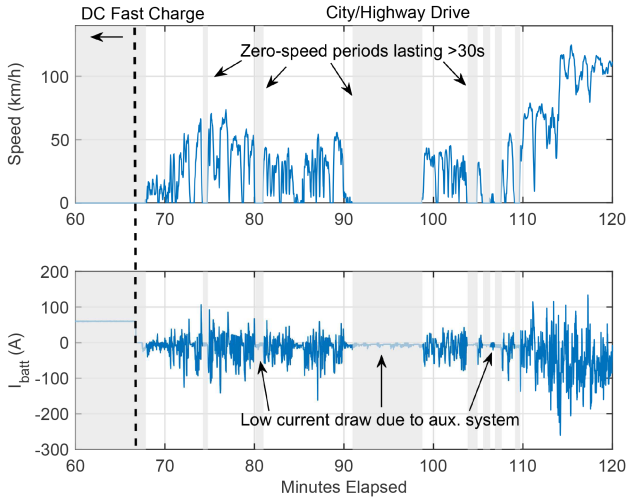

Fig. 4. Measured dynamic battery pack current from a GM Bolt, highlighting >30 s windows-of-opportunity for in-situ EIS, where battery current is near-zero.

The measured impedance of a 44Ah lithium nickel manganese cobalt oxide (NMC) battery cell at various temperatures is shown in Fig. 3(b). The cell impedance must be modeled across a temperature range due to the high sensitivity.

The impedance data utilized for ECM extraction is typically obtained through EIS, wherein the battery is exposed to a sinusoidal voltage or current perturbation, and the corresponding current or voltage response is measured [11]. Phasor calculations are then performed to obtain the impedance across a frequency range. The ECM parameters are subsequently obtained through curve-fitting to generate the best match at individual operating conditions [12], [13], [14]. In-situ EIS, where the battery impedance is characterized in real time, is motivated by the difficulty of modeling the nonlinear impedance degradation unique to each EV lifetime use-case. Capacity and impedance degradation are functions of temperature, depth-of-discharge, and the charge/discharge profile [10]. The real-time impedance data can improve the BMS model and state estimation accuracy by reducing the reliance on time-domain model identification algorithms. In-situ EIS is limited by the allowable test duration during EV operation. For example, only three cycles of a 0.1 Hz purely-sinusoidal perturbation can fit into a 30 s window of zero EV speed. The dynamic operating current of a GM Bolt battery pack is shown in Fig. 4, highlighting the windows-of-opportunity to perform in-situ EIS. By measuring within these time windows, a database of impedance phasors at arbitrary temperature, SOC, and degradation states can be periodically updated.

In the EV application, battery impedances reach below 1 mΩ, which yields small voltage responses (<10 mV) to practical perturbation currents (<10 A). Increasing the perturbation current amplitude yields improved signal-to-noise ratio (SNR) for the same test duration, but also increases the power electronics hardware cost. Therefore, it is crucial to design systems that are noise-tolerant, but do not introduce a significant hardware cost. Existing works on in-situ EIS have primarily been focused on the system implementation. Power electronics topologies have been introduced to address the added hardware cost of in-situ EIS [15], [16], [17], [18], [19], [20]. Broadband perturbation signal patterns that combine multiple frequencies into a single test have been proposed to improve the information density of measured data [21], [22]. Little work exists where data is extracted from the measured impedance for eventual use in an EV BMS. Examples include [23], where the battery impedance is correlated to a precharacterized internal temperature. In [24], the impedance data is used for SOH estimation with predefined health-factors that examine the geometric features of the impedance Nyquist curve. So far, no analysis has been done to quantify the ECM extraction accuracy under real-world impedance measurement inaccuracy. The impact of ECM accuracy on the SOP/SOC estimation accuracy, and ultimately the virtual loss of battery performance, has also not been quantified.

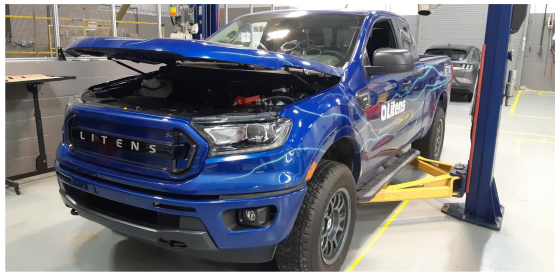

Fig. 5. Prototype electric truck where the in-situ EIS system is deployed.

The two primary contributions of this work are as follows: 1) The pack-level discharge energy versus SOP/SOC estimation errors is simulated, providing insight into the ECM accuracy required to avoid significant virtual loss of battery performance, and 2) the measured-impedance error tolerance of three common ECM extraction techniques is examined through a randomized set of simulated EIS tests with injected measurement noise. The work is validated using an EV-scale in-situ EIS platform designed for the electrified Ford Ranger pickup of Fig. 5, where large-scale impedance measurement is demonstrated for the first time. The *eTruck* is fitted with custom BMS and EIS systems which enable the use of a Tesla Model 3 battery pack, as discussed in [25]. In-situ impedance measurement is performed on 20 battery submodules and 53 ECMs are evaluated for accuracy.

II. In-Situ EIS System Architecture

The in-situ EIS system discussed in this work is shown in Fig. 6 and the hardware operation is discussed in more detail in [25]. The 400-to-12 V dc–dc converter is implemented with a triple-active-bridge (TAB) topology. The TAB provides low-voltage power to the EV 12 V auxiliary system in normal operation, and can be operated to perform EIS current perturbation between the two high-voltage battery half-packs. With the multimode TAB operation, in-situ EIS is introduced at a low incremental hardware cost.

The signal processing architecture of the in-situ EIS system is shown in Fig. 7. The EIS voltage response measurement

Authorized licensed use limited to: Sungkyunkwan University. Downloaded on August 18,2025 at 04:23:47 UTC from IEEE Xplore. Restrictions apply.

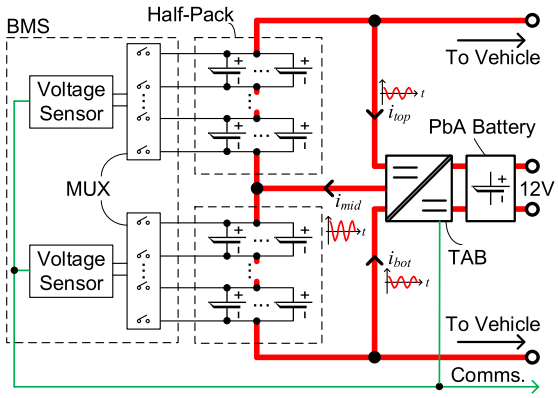

Fig. 6. In-situ EIS system architecture.

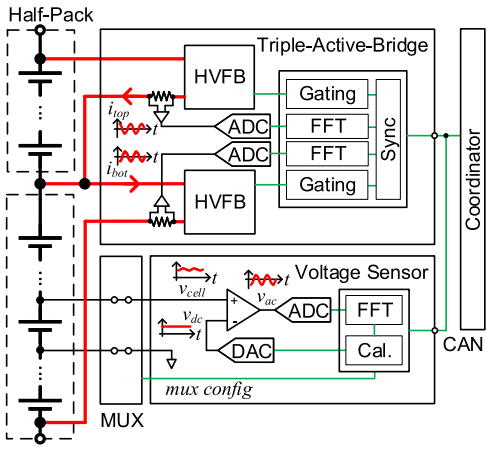

Fig. 7. Signal processing architecture of the in-situ EIS system.

occurs at the submodule-level, and the required number of voltage-sensing channels is reduced by multiplexing multiple battery submodule voltages to a single sensor. The EIS perturbation current is sampled by the same sensor used in the TAB current perturbation control system. The perturbation-current and response-voltage phasors are obtained by extracting the harmonic component corresponding to the perturbation frequency from a fast Fourier transform (FFT) of the sampled signals. In this work, the TAB operates with a 5A-peak sinusoidal perturbation current, and the rated battery capacity is above 200 Ah, thus, the EIS C-rate is 0.025 C.

The voltage and current measurements are synchronised by a coordinator through a 500 kb/s controller area network (CAN) communication interface. Each frequency in the EIS sweep is initiated by a trigger message frame broadcast on the CAN bus. Based on the system architecture, the sources of disturbance that might impact the impedance measurement accuracy include the following:

1) current disturbance from the loads/sources connected to the HV battery, which are somewhat controllable during the zero-speed in-situ EIS opportunities highlighted in Fig. 4;
2) measurement noise in the current and voltage sensing modules, which is one research focus of this work;
3) phase-angle distortion due to measurement sample timing mismatch, which is negligible due to the high-frequency embedded system operation.

Even if microsecond-scale delays occur due to signal propagation, they are short compared to the minimum perturbation period (0.5 ms in this work), and they do not accumulate.

III. SOP/SOC Estimation Sensitivity Analysis

The virtual loss of performance in an EV battery pack can be quantified by examining the condition where the discharge is limited by the BMS-estimated SOP/SOC. Based on the ECM of Fig. 1(b), the battery submodule current is limited by the following:

1) manufacturer-specified terminal voltage limits, which apply to v_n;
2) the heat generated in the submodule, which is a function of the current, i_p, and impedance, Z_n;
3) the SOC-dependent submodule EMF, V_{OC};
4) the voltage-to-current response as indicated by the submodule impedance.

The instantaneous electrically limited SOP of a battery pack during discharge is expressed as

$$\mathrm{SOP} = i_{\max} \sum_{n=1}^{N} v_n \tag{1}$$

where v_n is the nth submodule in the battery stack, and $i_{\max}$ is the current that results in the voltage-limited submodule reaching the maximum-allowable terminal voltage, $V_{\max}$. In the presence of capacity and impedance imbalance, not all submodules necessarily reach the maximum voltage simultaneously. The expression for $i_{\max}$ varies with the specific impedance elements used to model the battery. In the general case of Fig. 1(b), assuming a short discharge time window where V_{OC} does not change significantly, the maximum battery current is expressed implicitly as

$$V_{\mathrm{OC}} + v_Z(i_{\max}) = V_{\max} \tag{2}$$

where v_Z is the time-varying voltage of the lumped ECM elements, and is dependent on the arbitrary pack current prior to the estimation instance. A similar analysis applies for the discharge scenario.

The SOP definition of (2) provides only the instantaneous value, whereas it is common in practice to estimate SOP for a range of time-horizons. A power-limited operating scenario measured in a commercial EV is shown in Fig. 8. The logged battery power, discharge SOP limit, and regenerative braking SOP limit are shown in Fig. 8(a). Multiple high-power regenerative braking events momentarily exceed the SOP limit. Corresponding overvoltage events are seen in Fig. 8(b), which shows the maximum and minimum cell voltages in the pack over the same time period. This is an example of applying a conservative voltage limit to provide safety margin against erroneous SOP estimates. The logged data also demonstrates that SOP prediction horizons must accommodate near-instantaneous values to accommodate regenerative braking events. In this work, it is assumed that SOP estimation accuracy is fundamentally limited by

Authorized licensed use limited to: Sungkyunkwan University. Downloaded on August 18,2025 at 04:23:47 UTC from IEEE Xplore. Restrictions apply.

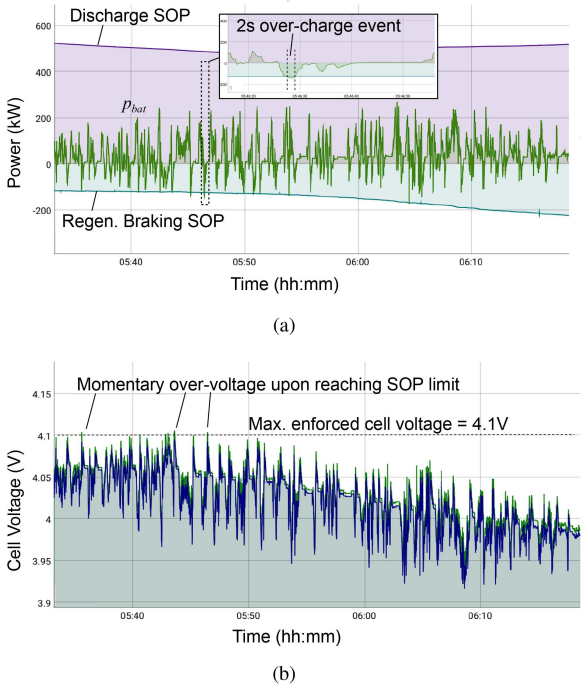

Fig. 8. Logged data from an commercial EV driving from 100% SOC. (a) Battery power and the charge and discharge SOP limits. (b) Minimum and maximum cell voltages over the same period.

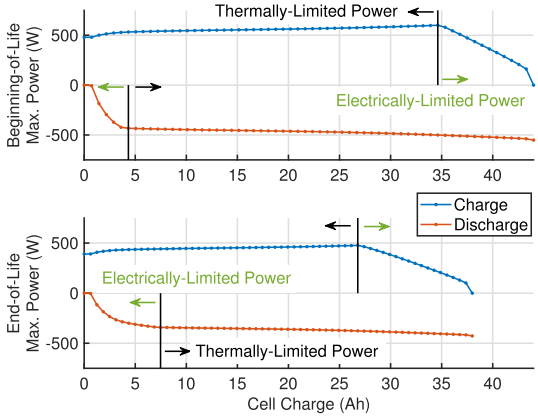

Fig. 9. Maximum charge/discharge power of a 44-Ah-nominal lithium NMC cell in an EV application, shown for the beginning-of-life (100% SOH), and near the EOL (86% SOH).

the model accuracy. This includes cases such as [26], where the model time-dependence is factored into the prediction horizon. A detailed analysis of different SOP estimation algorithms is outside the scope of this work.

A sample 44-Ah Lithium NMC cell SOP curve is shown in Fig. 9. The operating limits are computed through a 1R-ECM, where the battery impedance, Z_n, is represented by a single resistor. The thermally limited SOP is based on a 50 W maximum heat dissipation enabled by a cooling system, and the electrically limited SOP is based on (2). Heat generation is obtained as the dissipation across the ECM resistance. At the end of charge and discharge, the SOP is typically electrically limited, therefore only the electrically-limited SOP is examined in this work.

Despite the advantage of up-to-date impedance measurements, in-situ EIS suffers from accuracy limitations due to the relatively-low response-voltage SNR achievable inside an EV, compared to a bench setup. An additional challenge is the lack of a reference impedance through which the in-situ EIS system can be calibrated during deployment. In this work, a relative-error metric is used to quantify the relative performance of a 1R-ECM with the resistance value obtained from different sources. A 1R-ECM is used in the analysis to obtain meaningful insights without complex derivations. The metric is based solely on the measured-versus-ECM-predicted terminal voltage error, Δv_n. Under the 1R-ECM, the erroneous predicted submodule terminal voltage is expressed as

$$\hat{v_n} = v_{\text{OC}}(\text{SOC}) + i_p R_n(1+\epsilon_n) \qquad \epsilon_n > -1 \qquad \epsilon_n \neq 0 \tag{3}$$

where ϵ_n is the resistance error. Assuming the predicted SOC is the same under all 1R-ECM parameter sets in consideration, the voltage error is expressed as

$$\Delta v_n = i_p R_n \epsilon_n. \tag{4}$$

A negative error means the overpotential is underestimated, which leads to an overestimated SOP. Similarly, a positive error means the overpotential is overestimated, which leads to an underestimated SOP. The relative error between two candidate ECMs, ϵ_r, is defined as the error ratio between the ECMs, expressed as

$$\epsilon_r \triangleq \frac{\epsilon_2}{\epsilon_1} = \frac{\Delta v_2}{\Delta v_1}. \tag{5}$$

Finally, the impact of voltage estimation error on the SOP prediction is captured by forward-propagating the estimation error, ϵ_n, to the SOP, and assuming no SOC error. The erroneous SOP prediction is expressed as

$$\hat{\text{SOP}}_n = \frac{1}{(1+\epsilon_n)}\text{SOP} \tag{6}$$

where $\hat{\text{SOP}}_n$ is the erroneous SOP estimate.

A. BMS-Limited Battery Pack Simulation

A transient simulation was implemented to analyze the sensitivity of the battery pack discharge energy, E_{dchg}, to the BMS SOP/SOC estimation error. Multiple trials of the same discharge power profile were applied to a 12S4P, 176Ah down-scaled battery pack, and the operating temperature was swept from 0 to 30 °C. The SOP estimation error was introduced by applying a 0%–20% decrease to the true value calculated through (1) at each simulation time-step, using a 2RC ECM. The SOC estimation error was introduced by applying a 0%–10% decrease to the true simulated value. The introduction of erroneously-low SOP/SOC estimates leads to the underutilization of the battery pack energy storage capacity. This simulation therefore quantifies the relationship between the BMS model/estimation error and the virtually lost battery energy storage capacity.

Authorized licensed use limited to: Sungkyunkwan University. Downloaded on August 18,2025 at 04:23:47 UTC from IEEE Xplore. Restrictions apply.

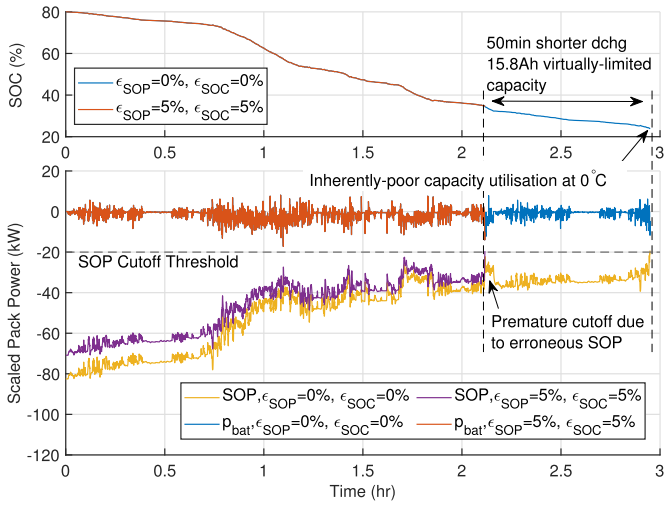

Fig. 10. Transient simulation of the scaled battery pack at 0 °C, highlighting the virtual loss of performance due to SOP/SOC error.

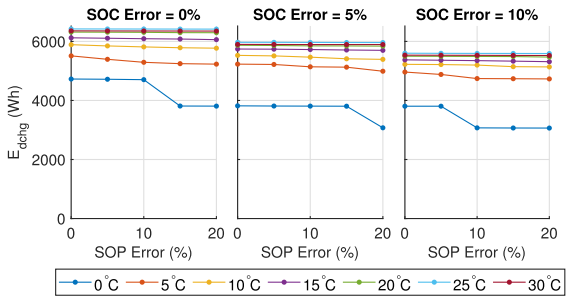

(a)

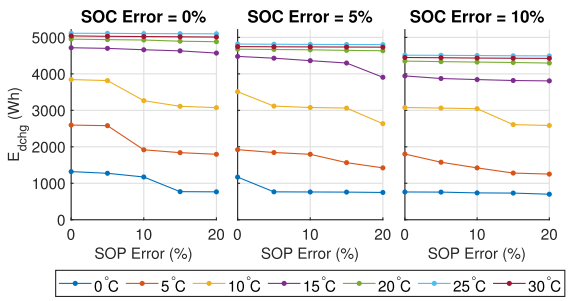

(b)

Fig. 11. Scaled battery pack E_{dchg} from a sweep of SOP/SOC error values from 0 to 30 °C. (a) Beginning-of-life (BOL), and (b) EOL.

A sample transient simulation instance is shown in Fig. 10 to highlight the SOP-based discharge termination. Compared to the zero-error case (blue), the 5% SOP/SOC error case (red) results in a premature termination by 50 min, with an extra 15.8 Ah discharge capacity remaining in the scaled pack. The EV-level impact is a reduced pack energy capacity, which corresponds to reduced range for the same discharge power rating.

Aggregated E_{dchg} results from the parameterized transient simulations are shown in Fig. 11. In the end-of-life (EOL) case, the batteries are modeled with a 20% decrease in Ah-capacity and 100% increase in total resistance. It can be seen that the E_{dchg} is the most sensitive to SOP/SOC estimation error below 10 °C and at the EOL, losing up to 50% of the total discharge capacity due to estimation error alone. It can be concluded that the BMS state estimation accuracy must be prioritized at low temperature and EOL conditions.

IV. ECM Extraction Noise Sensitivity

The analysis presented through (1)–(6) indicates that the SOP estimation accuracy is dependent on the ECM accuracy. Ultimately, in an in-situ EIS system, the extracted ECM accuracy is a function of both the hardware and software design. The hardware metrics focus predominantly on the impedance phasor measurement accuracy, whereas the software metrics consist of solely the ECM extraction process, which generates ECM parameters from the measured impedance phasors. Three candidate ECM extraction techniques for in-situ deployment are evaluated in this work according the sensitivity of extracted-ECM error to the input impedance phasor measurement noise. The evaluated techniques are as follows.

1) A phasor algebra method that obtains key features of a Nyquist curve (peaks and troughs of semicircles and slope identification at low-frequency), and approximates the ECM parameters through direct calculation, as shown in Fig. 12(a), and discussed in [12].
2) The circle-fit method, where the same Nyquist curve features as phasor algebra are used, but semicircle fitting occurs on all data-points within the relevant frequency ranges isolated by the peak and trough features, as shown in Fig. 12(b), and discussed in [13].
3) The complex nonlinear least-squares (CNLS) method, where iterative curve-fitting is applied across the entire frequency range, as shown in Fig. 12(c), and discussed in [14].

A. Measurement Error Sensitivity Analysis

The ECM extraction error sensitivity was carried out according to the method described in Fig. 13. Measured impedance data from a custom reference EIS setup was obtained and a baseline ECM was fitted using CNLS. Randomized EIS measurements were then simulated with the baseline ECM. Additive white Gaussian noise was introduced in the time domain with varying power levels to vary the impedance measurement SNR. An FFT was applied to the noisy current and voltage samples, using a buffer size of 1024 samples, which reflects the system presented in Fig. 7. The resulting noisy impedance, Z_{noise}, was finally passed to the ECM extraction stage, and the output noisy ECM parameters were compared to the manually fitted reference. A total of 100 trials were performed for each SNR value and ECM extraction method, and the full analysis consists of 30 000 simulated EIS and ECM extraction scenarios.

The aggregated fitting results using the three ECM extraction methods are shown in Fig. 14. A mean (lines) and standard deviation (1σ vertical bars) are reported for each extraction method, SNR value, and ECM parameter. The phasor algebra fit, as shown in Fig. 14(a), results in a dramatic increase in the C_1 error percentage as SNR reduces below 40 dB. There

Authorized licensed use limited to: Sungkyunkwan University. Downloaded on August 18,2025 at 04:23:47 UTC from IEEE Xplore. Restrictions apply.

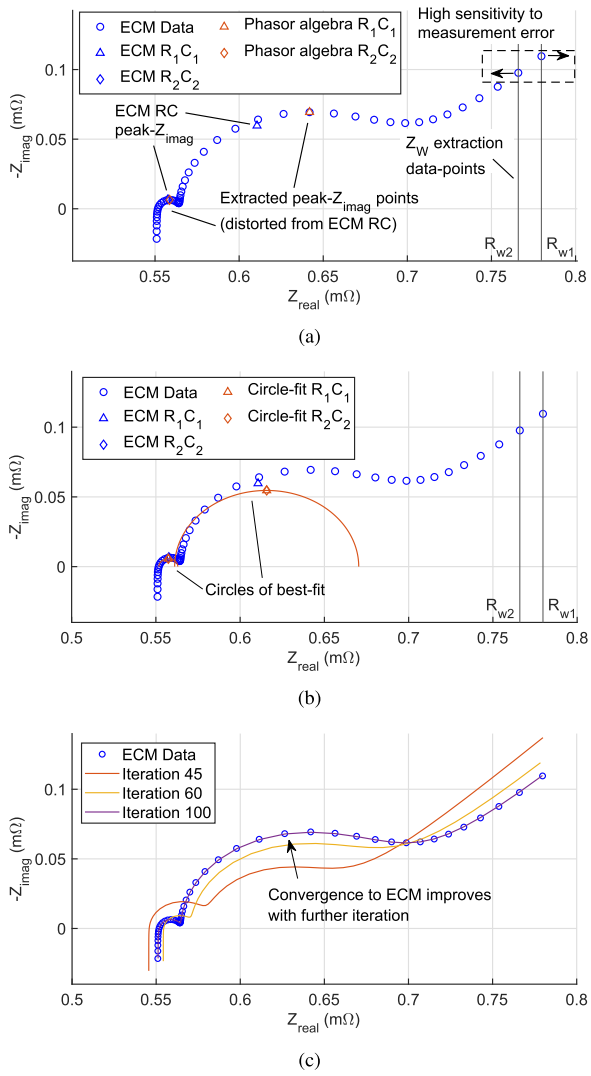

Fig. 12. The ECM extraction methods analysed in this work for sensitivity to input impedance error: (a) Phasor algebra, (b) Circle fit, and (c) CNLS.

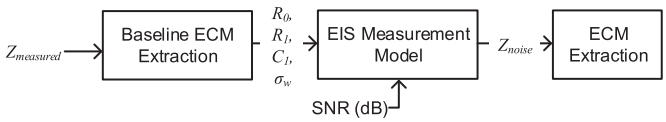

Fig. 13. Measurement error simulation model.

also exists a steady error in the R_1 and C_1 values as SNR approaches 100 dB. These characteristics are a result of the phasor algebra method utilising only single-frequency data-points that represent the peak and trough features of the Nyquist curve, as shown in Fig. 12(a). The phasor algebra extraction accuracy is therefore highly-sensitive to impedance measurement error. The circle-fit extraction results, as shown in Fig. 14(b), resemble the results of the phasor algebra method, but with smaller-magnitude ECM parameter errors. This is due to an error-averaging effect achieved through the use of multiple impedance data-points within the circular regions of the Nyquist curve. The CNLS

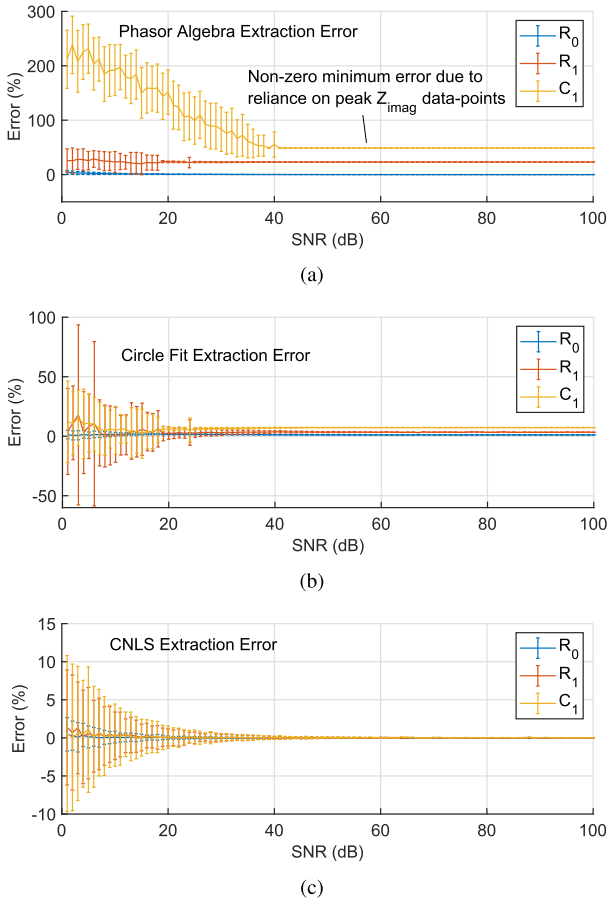

Fig. 14. Aggregated fitting results using the three ECM extraction methods (error bar denotes standard deviation). (a) Phasor algebra. (b) Circle-fit. (c) CNLS.

method, as shown in Fig. 14(c), was found to be the most noise-immune algorithm among the three, and the most promising selection for in-situ EIS. The average computation times were 0.24 ms, 0.37 ms, and 5.05 ms for the phasor algebra, circle-fit, and CNLS, respectively, which highlights the error versus computational-effort tradeoff.

V. Experimental Results

The eTruck in-situ EIS system test setup is shown in Fig. 15. The Model 3 battery packs are retrofitted with a custom BMS and the EIS system of Figs. 6 and 7. The experimental focus of this work is on the large-scale impedance measurement of 20 submodules across the battery pack from 0 to 25 °C. The battery temperature was varied using a thermal chamber, and the battery pack was then deployed in the eTruck of Fig. 5 for voltage measurement while driving.

The measured in-situ impedance of 20 submodules from the eTruck battery pack are shown in Fig. 16. Two EIS sweeps were performed for each submodule at 0 °C, 10 °C, and 25 °C, and a frequency range from 0.059 to 1952 Hz. A total of 3080 single-frequency impedance data points were collected. Among the collected data, 20% of the single-frequency impedance points were classified as outliers due to their values falling outside

Authorized licensed use limited to: Sungkyunkwan University. Downloaded on August 18,2025 at 04:23:47 UTC from IEEE Xplore. Restrictions apply.

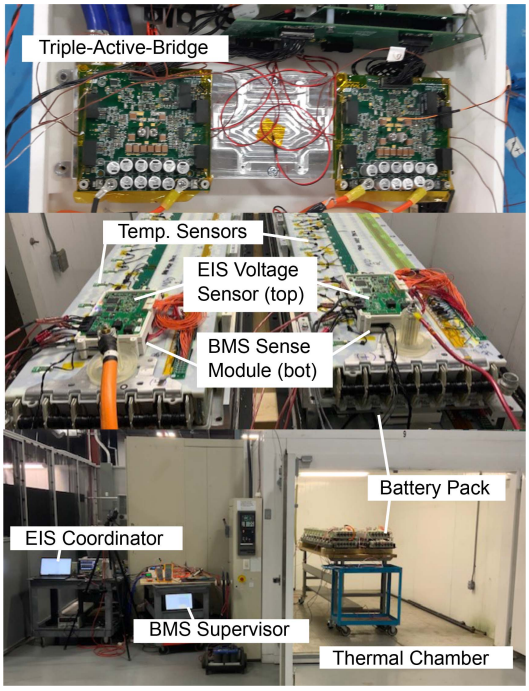

Fig. 15. eTruck in-situ EIS system thermal chamber test setup for temperature-controlled impedance measurements.

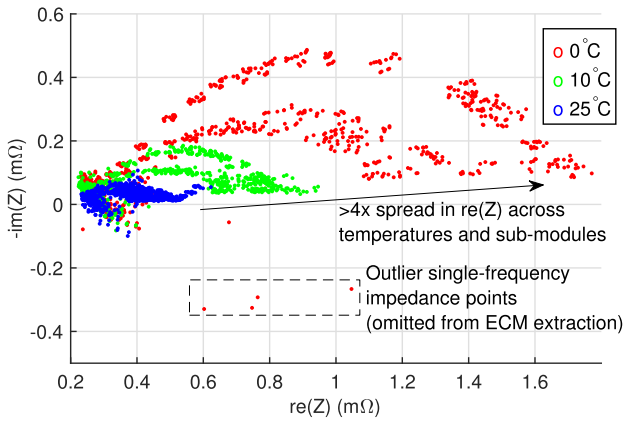

Fig. 16. Nyquist plot of 2464 impedance measurements from 20 submodules obtained from the in-situ EIS system.

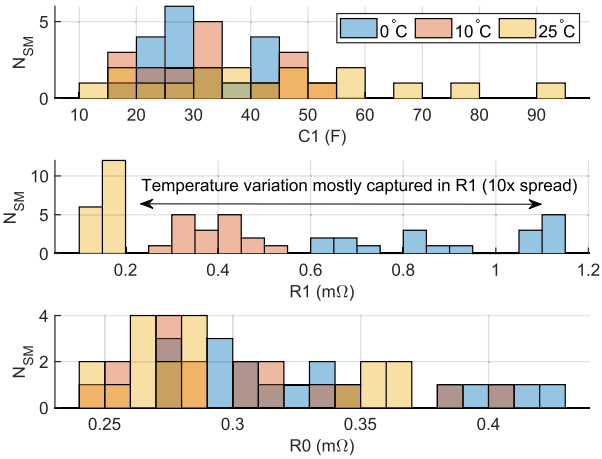

Fig. 17. Distribution of extracted ECM parameters from 18 submodules at 0 °C, 10 °C, and 25 °C. The number of submodules is denoted N_{SM}.

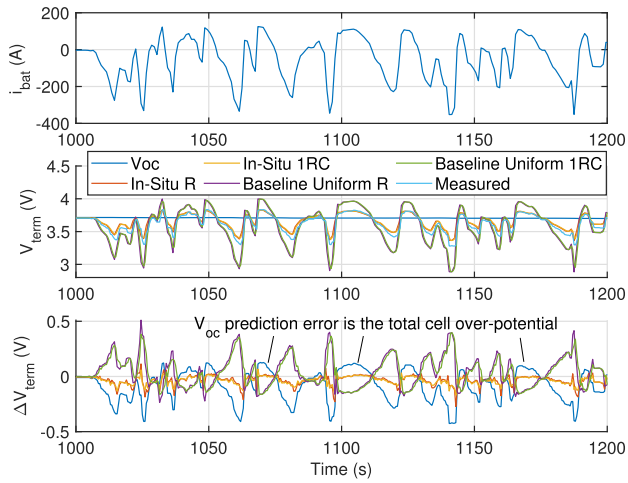

Fig. 18. Comparison between the measured terminal voltage of a single submodule and the simulated response of v_{oc}, 1R, and 1RC-ECMs at 3 °C.

the real and imaginary impedance range of [0.2, 1.8] m Ω and [−0.2, 0.8] mΩ, respectively. The outlier data points occurred due to low-temperature component variation in the voltage measurement circuit. The outlier data was not utilized for ECM extraction, leading to the omission of 2 submodules from further analysis at 0 ° C, and 3 submodules from further analysis at 10 °C. The temperature dependence of battery electrical behavior is observed in the four-times real-impedance spread across the temperature range.

The measured impedance data was used to generate 1RC ECMs for the individual submodules using the CNLS method for maximum accuracy. The distribution of ECM parameters across submodules for each temperature is shown in Fig. 17. The Ohmic resistance (R0) exhibits a two-times spread across the temperature range, whereas the R1 parameter varies by five-times. This is likely due to the strong temperature dependence of the charge transfer impedance inside the battery cells. While the C1 parameter varies by two-times more at 25 °C compared to other temperatures, the overall impact on submodule impedance variation is reduced at 25 °C due to a significantly-lower R1 value.

The extracted ECMs were simulated with measured data from multiple driving tests to quantify the voltage prediction error across a temperature range. The measured eTruck data, all for a single submodule, are shown in Fig. 18. The battery EMF voltage, V_{OC}, is plotted and compared against the measured terminal voltage V_{term} to represent the total submodule overpotential [V_Z of Fig. 1(b)]. The baseline uniform ECM is obtained from a representative Tesla 2170 battery cell, with impedance measured on the bench and ECM extracted using CNLS. The baseline uniform ECM was applied to all submodules in the error analysis, whereas the in-situ ECMs were unique to each submodule. The baseline uniform models exhibit a peak error magnitude of 0.5 V at 1025 s, while the in-situ models exhibit a peak error magnitude of 0.27 V at 1143 s.

Authorized licensed use limited to: Sungkyunkwan University. Downloaded on August 18,2025 at 04:23:47 UTC from IEEE Xplore. Restrictions apply.

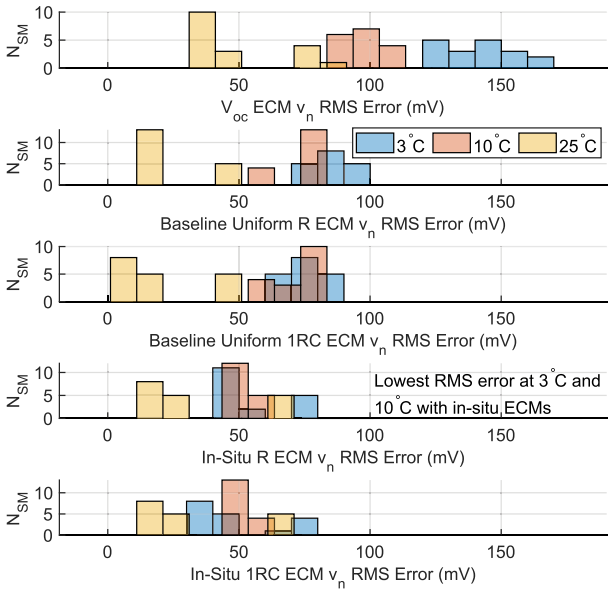

Fig. 19. Distribution of the rms error between the measured terminal voltage of selected submodules from the pack and the respective v_{oc}, 1R, and 1RC ECMs, from 3 to 25 °C.

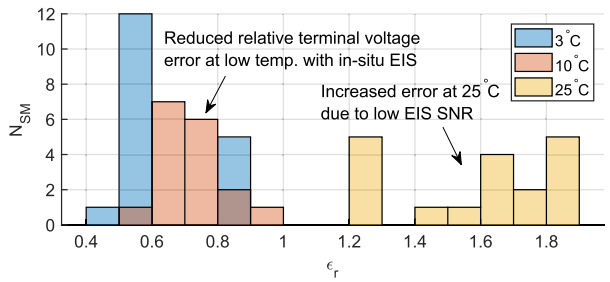

Fig. 20. Distribution of the relative voltage prediction error ϵ_r between the baseline 1R-ECMs and in-situ 1R-ECMs.

The rms error distribution between the measured and predicted voltages of each submodule for the three temperature scenarios are shown in Fig. 19. In total, 53 comparisons using the in-situ extracted ECMs were performed across all submodules and temperatures. The cell overpotential provides an upper bound for the error magnitude that the ECM predictions should stay within. The in-situ ECMs generally predict the submodule voltages at 20–30 mV below the baseline ECM RMS error at 3 °C and 10 °C, where the battery pack performance is most sensitive to SOP estimation error.

The distribution of relative rms voltage prediction error values between the in-situ and baseline 1R-ECMs for each submodule is shown in Fig. 20. The relative error, ϵ_r is below 1 in all cases at 3 °C and 10 °C. This highlights the superiority of the in-situ model in estimating the battery overpotential.

The raw model error and SOP accuracy are summarized in Table I. The error values, denoted ϵ_n, are obtained from the portion of overpotential that is not predicted by each ECM. The mean ϵ_n values are obtained from all in-situ extracted ECMs. The SOP estimation error ratio, $\hat{\text{SOP}}/\text{SOP}$, is then calculated according to (6). The SOP estimation accuracy improvement

TABLE I
MODEL ERROR AND ESTIMATED SOP ACCURACY

Temp. (°C)	Baseline 1R-ECM		In situ 1R-ECM	
	ϵ_n	SOP/SOP	Mean ϵ_n	Mean SOP/SOP
3	0.59	0.63	0.38	0.72
10	0.76	0.57	0.54	0.65
25	0.46	0.68	0.73	0.58

with in-situ EIS is approximately 8% at 10 °C and 9% at 3 °C (ϵ_n decreases, and SOP accuracy improves). As shown in Figs. 10 and 11, the pack discharge energy is most sensitive to SOP estimation error below 10 °C. The SOP estimation error at 25 °C, therefore, has a low impact on EV range. These results indicate that in-situ EIS can reduce the virtual loss of battery performance by improving the submodule ECM accuracy.

VI. CONCLUSION

An EV-scale in-situ EIS system was demonstrated in this work. The SOP and SOC estimation error was found to impact the battery discharge energy most significantly at low temperature and the end-of-life. A simulation-based noise-sensitivity analysis of three ECM extraction techniques was conducted. It was found that ECM extraction using single-frequency datapoints is the most sensitive to impedance measurement error. The fully iterative CNLS method resulted in a bounded ECM extraction error of +/−10% as the SNR was decreased to 1 dB. Experimental validation of 53 extracted ECMs across 18 battery submodules was performed using a custom in-situ EIS system and measured data from an EV. The SOP estimation accuracy improved by 8%–9% at 3 °C and 10 °C between the in-situ extracted ECMs and a representative bench-top baseline. This work is the first-known demonstration of in-situ EIS and ECM extraction at the EV scale in the literature. The results show that in-situ EIS and ECM extraction have the potential to improve EV BMSs by decreasing the virtual loss of battery performance.

ACKNOWLEDGMENT

The authors would like to thank all team members from Litens Automotive Partnership, including Alex, Ali, Anthony, Brad, Deqiang, Milan, and Noel for their technical contributions to the project. The authors also would like to thank Andrew, Geoffrey, and Sean for their continued support of the research collaboration and M. Fard for his telematics data contributions.

REFERENCES

[1] "Global EV outlook 2022," 2022. [Online]. Available: https://www.iea.org/reports/global-ev-outlook-2022

[2] W. Waag, C. Fleischer, and D. U. Sauer, "Critical review of the methods for monitoring of lithium-ion batteries in electric and hybrid vehicles," *J. Power Sources*, vol. 258, pp. 321–339, 2014, doi: 10.1016/j.jpowsour.2014.02.064.

[3] G. Xianzhi and C. C. Mi, "Temperature-dependent performance of lithium ion batteries in electric vehicles," in *Proc. IEEE Appl. Power Electron. Conf. Expo.*, 2015, pp. 1065–1072, doi: 10.1109/APEC.2015.7104480.

[4] A. Moshirvaziri, J. Liu, Y. Arumugam, and O. Trescases, "Modelling of temperature dependent impedance in lithium ion polymer batteries and impact analysis on electric vehicles," in *Proc. IECON 40th Annu. Conf. IEEE Ind. Electron. Soc.*, 2014, pp. 3149–3155, doi: 10.1109/IECON.2014.7048960 .

Authorized licensed use limited to: Sungkyunkwan University. Downloaded on August 18,2025 at 04:23:47 UTC from IEEE Xplore. Restrictions apply.

[5] J. Cao, N. Schofield, and A. Emadi, "Battery balancing methods: A comprehensive review," in *Proc. IEEE Vehicle Power Propulsion Conf.*, 2008, pp. 3–8, doi: 10.1109/VPPC.2008.4677669.
[6] "Bolt EV recall," 2021. [Online]. Available: https://my.gm.ca/chevrolet/en/how-to-support/safety/boltevrecall
[7] M. Andersson, M. Johansson, and V. L. Klass, "A continuous-time LPV model for battery state-of-health estimation using real vehicle data," in *Proc. IEEE Conf. Control Technol. Appl.*, 2020, pp. 692–698, doi: 10.1109/CCTA41146.2020.9206257.
[8] M. A. Xavier, A. K. de Souza, and M. S. Trimboli, "An LPV-MPC inspired battery sop estimation algorithm using a coupled electro-thermal model," in *Proc. Amer. Control Conf.*, 2021, pp. 4421–4426, doi: 10.23919/ACC50511.2021.9483433.
[9] H. Rahimi-Eichi, F. Baronti, and M.-Y. Chow, "Online adaptive parameter identification and state-of-charge coestimation for lithium-polymer battery cells," *IEEE Trans. Ind. Electron.*, vol. 61, no. 4, pp. 2053–2061, Apr. 2014, doi: 10.1109/TIE.2013.2263774.
[10] D. Galatro, M. Al-Zareer, C. Da Silva, D. Romero, and C. Amon, "Thermal behavior of lithium-ion batteries: Aging, heat generation, thermal management and failure," *Front. Heat Mass Transfer*, vol. 14, 2020, doi: 10.5098/hmt.14.17.
[11] S. Buller, M. Thele, R. W. A. A. D. Doncker, and E. Karden, "Impedance-based simulation models of supercapacitors and li-ion batteries for power electronic applications," *IEEE Trans. Ind. Appl.*, vol. 41, no. 3, pp. 742–747, May 2005, doi: 10.1109/TIA.2005.847280.
[12] S. R. Islam, S.-Y. Park, and B. Balasingam, "Circuit parameters extraction algorithm for a lithium-ion battery charging system incorporated with electrochemical impedance spectroscopy," in *Proc. IEEE Appl. Power Electron. Conf. Expo.* 2008, pp. 3353–3358.
[13] K. Kanatani and P. Rangarajan, "Hyper least squares fitting of circles and ellipses," vol. 55, no. 6, pp. 2197–2208, 2011, doi: https://doi.org/10.1016/j.csda.2010.12.012. [Online]. Available: https://www.sciencedirect.com/science/article/pii/S0167947310004809
[14] B. A. Boukamp, "A nonlinear least squares fit procedure for analysis of immittance data of electrochemical systems," *Solid State Ionics*, vol. 20, no. 1, pp. 31–44, 1986, doi: https://doi.org/10.1016/0167-2738(86)90031-7. [Online]. Available: https://www.sciencedirect.com/science/article/pii/0167273886900317
[15] Y. Elasser, Y. Chen, M. Liu, and M. Chen, "A multiway bidirectional multiport-ac-coupled (MAC) battery balancer with online electrochemical impedance spectroscopy," in *Proc. IEEE Appl. Power Electron. Conf. Expo.*, 2020, pp. 1475–1482, doi: 10.1109/APEC39645.2020.9124422.
[16] A. Kersten et al., "Online and on-board battery impedance estimation of battery cells, modules or packs in a reconfigurable battery system or multilevel inverter," in *Proc. IECON 46th Annu. Conf. IEEE Ind. Electron. Soc.*, 2020, pp. 1884–1891, doi: 10.1109/IECON43393.2020.9254515.
[17] E. Din, C. Schaef, K. Moffat, and J. T. Stauth, "A scalable active battery management system with embedded real-time electrochemical impedance spectroscopy," *IEEE Trans. Power Electron.*, vol. 32, no. 7, pp. 5688–5698, Jul. 2017, doi: 10.1109/TPEL.2016.2607519.
[18] Y. D. Lee, S. Y. Park, and S. B. Han, "Online embedded impedance measurement using high-power battery charger," *IEEE Trans. Ind. Appl.*, vol. 51, no. 1, pp. 498–508, Jan. 2015, doi: 10.1109/TIA.2014.2336979.
[19] Z. Gong et al., "IC for online EIS in automotive batteries and hybrid architecture for high-current perturbation in low-impedance cells," in *Proc. IEEE Appl. Power Electron. Conf. Expo.*, 2018, pp. 1922–1929, doi: 10.1109/APEC.2018.8341280.
[20] J. Shen, H. Homayouni, and J. Wang, "Converter-based electrochemical impedance spectroscopy for high-power fuel cell stacks with resonant controllers," *IEEE Trans. Ind. Electron.*, vol. 68, no. 9, pp. 8819–8828, Sep. 2021, doi: 10.1109/TIE.2020.3016250.
[21] S. Nejad and D. T. Gladwin, "Online battery state of power prediction using PRBs and extended Kalman filter," *IEEE Trans. Ind. Electron.*, vol. 67, no. 5, pp. 3747–3755, May 2020, doi: 10.1109/TIE.2019.2921280.
[22] C. de Beer, P. S. Barendse, and P. Pillay, "Fuel cell condition monitoring using optimized broadband impedance spectroscopy," *IEEE Trans. Ind. Electron.*, vol. 62, no. 8, pp. 5306–5316, Aug. 2015, doi: 10.1109/TIE.2015.2418313.
[23] L. H. J. Raijmakers, D. L. Danilov, J. P. M. van Lammeren, T. J. G. Lammers, H. J. Bergveld, and P. H. L. Notten, "Non-zero intercept frequency: An accurate method to determine the integral temperature of li-ion batteries," *IEEE Trans. Ind. Electron.*, vol. 63, no. 5, pp. 3168–3178, May 2016, doi: 10.1109/TIE.2016.2516961.
[24] Y. Fu, J. Xu, M. Shi, and X. Mei, "A fast impedance calculation-based battery state-of-health estimation method," *IEEE Trans. Ind. Electron.*, vol. 69, no. 7, pp. 7019–7028, Jul. 2022, doi: 10.1109/TIE.2021.3097668.
[25] S. A. Assadi et al., "In-situ EV battery electrochemical impedance spectroscopy with pack-level current perturbation from a 400V-to-12V triple-active-bridge," in *Proc. IEEE Appl. Power Electron. Conf. Expo.*, 2022, pp. 1056–1063, doi: 10.1109/APEC43599.2022.9773622.
[26] P. Malysz, J. Ye, R. Gu, H. Yang, and A. Emadi, "Battery state-of-power peak current calculation and verification using an asymmetric parameter equivalent circuit model," *IEEE Trans. Veh. Technol.*, vol. 65, no. 6, pp. 4512–4522, 2016, doi: 10.1109/TVT.2015.2443975.

Zhe Gong (Member, IEEE) received the M.A.Sc degree in electrical engineering in 2018 from the University of Toronto, Toronto, ON, Canada, where he is currently working toward the Ph.D. degree in electrical engineering.

His research focuses on electric vehicle battery systems.

Avram Kachura received the B.A.Sc degree in engineering science in 2022 from the University of Toronto, Toronto, ON, Canada, where he is currently working toward the M.A.Sc. degree in electrical engineering.

His main research interests include robotics, energy storage technology, and Li-Ion battery modeling.

Seyed Amir Assadi (Student Member, IEEE) received the B.A.Sc. and M.A.Sc. degrees in electrical engineering, in 2016 and 2019, respectively, from the University of Toronto, Toronto, ON, Canada, where he is currently working toward the Ph.D. degree in electrical engineering.

His research focuses on high density EV battery chargers.

Nicholas Cusimano received the B.A.Sc degree in computer engineering from the University of Toronto, Toronto, ON, Canada, in 2018.

Since 2018, he has been an Engineering Technologist with the University of Toronto Electric Vehicle Research Group, Toronto.

Joshua Piruzza is currently working toward the Undergraduate degree in electrical engineering with the University of Toronto, Toronto, ON, Canada.

He was with Peak Power and the University of Toronto Electric Research Center, Toronto.

Authorized licensed use limited to: Sungkyunkwan University. Downloaded on August 18,2025 at 04:23:47 UTC from IEEE Xplore. Restrictions apply.

James Xu is a currently working toward the Undergraduate degree in computer engineering with the University of Toronto, Toronto, ON, Canada.

He was a Research Assistant with the UTEV lab, University of Toronto from 2021 to 2022.

Olivier Trescases (Senior Member, IEEE) received the Ph.D. degree in electrical engineering from the University of Toronto, Toronto, ON, Canada.

He is currently a Professor with the Edward S. Rogers Sr. Department of Electrical and Computer Engineering, University of Toronto.

Dr. Trescases is currently a Canada Research Chair in Power Electronic Converters and a Past Chair of the IEEE Toronto Section. He has been an Associate Editor for the IEEE TRANSACTIONS ON POWER ELECTRONICS since 2015.

Authorized licensed use limited to: Sungkyunkwan University. Downloaded on August 18,2025 at 04:23:47 UTC from IEEE Xplore. Restrictions apply.